minerals

MDPI

Article

Formation of the Miaoan Au-Polymetallic Deposit in the Northern Taihang Mountain, North China Craton: Ore Geology, Geochronological and Geochemical Perspectives

Jie Li [1,2,3], Nan Li [1], Meiyun Wang [4], Yingxin Song [5], Zongyuan Tang [6], Pu Zhang [6], Guang Wang [7] and Lipeng Zhang [3,*]

1 Hebei Key Laboratory of Strategic Critical Mineral Resources, Hebei GEO University, Shijiazhuang 050031, China
2 Applied Nuclear Technology in Geosciences Key Laboratory of Sichuan Province, Chengdu University of Technology, Chengdu 610059, China
3 Center of Deep Sea Research, Institute of Oceanology, Chinese Academy of Sciences, Qingdao 266071, China
4 School of Water Resources and Environment, Hebei GEO University, Shijiazhuang 050031, China
5 Institute of Geological Sciences of Shandong Province, Jinan 250013, China
6 Institute of Geological Survey, Hebei GEO University, Shijiazhuang 050031, China
7 CNBM Geological Engineering Exploration Academy Co., Ltd., Beijing 100102, China
* Correspondence: zhanglipeng@qdio.ac.cn

Abstract: Several gold ore-concentrated areas have been recognized in the destruction zone of the North China Craton (NCC). However, the deposits in the western part of the destruction zone have received less attention. Miaoan, a typical Au-polymetallic deposit in the northern Taihang Mountain, provides a good sample for deepening our understanding of the genesis of gold deposits in the western destruction zone. In this study, detailed ore geology, pyrite Rb-Sr age, trace element and S-C-O isotopes of Au-bearing ores were conducted to constrain the source of ore-forming materials and their tectonic setting. The pyrites obtain an Rb-Sr isochron age of 129.5 ± 2.5 Ma, consistent with those of magmatic rocks in this deposit, suggesting their genetic relationship. The $\delta^{34}S$ values ranging from −5.5‰ to 1.6‰ and the high Co/Ni and Y/Ho ratios of pyrites indicate the mantle-crust mixing characteristics of ore-forming fluids. The $\delta^{13}C$ (−6.3‰ to −2.0‰) and $\delta^{18}O$ (9.3‰ to 17.6‰) values of Au-bearing ores and calcites suggest mixing characteristics as well. Geochronologically, the Miaoan Au-polymetallic deposit was formed during the destruction of the NCC. We propose that the Miaoan Au-polymetallic deposit is a decratonic gold deposit and that its ore-forming materials have a mixed source of mantle and crust.

Keywords: Miaoan Au-polymetallic deposit; S-C-O isotopes; pyrite Rb-Sr dating; northern Taihang Mountain; North China Craton

check for updates

Citation: Li, J.; Li, N.; Wang, M.; Song, Y.; Tang, Z.; Zhang, P.; Wang, G.; Zhang, L. Formation of the Miaoan Au-Polymetallic Deposit in the Northern Taihang Mountain, North China Craton: Ore Geology, Geochronological and Geochemical Perspectives. *Minerals* **2022**, *12*, 1144. https://doi.org/10.3390/min12091144

Academic Editor: Maria Boni

Received: 14 August 2022
Accepted: 6 September 2022
Published: 10 September 2022

1. Introduction

The margin of the craton is often abnormally rich in gold, molybdenum, and rare earth element (REE) deposits [1–4]. Several large-scale Au mineralization provinces formed around the NCC destruction zone during the Mesozoic, such as the Jiaodong, Xiaoqinling, Liaodong, and Jidong mineralization provinces [2,5–11]. The genesis of these Au deposits has received much attention, especially in the Jiaodong region [5,6,12–17]. Several models have been proposed, such as orogenic type, Jiaodong type, and decratonic type [2,3,15–23]. Addressing the genesis of these Au deposits may require looking at the issue from a broader perspective. Studies in recent years have shown that the northern Taihang Mountain (TM), west of the NCC destruction zone, developed a large number of gold deposits, such as the Shihu, Yixingzhai, Liyuan, and Gengzhuang gold deposits (Figure 1a). However, these deposits have received relatively less attention [13,24–27]. This is not conducive to understanding the genesis of Mesozoic gold deposits in the entire NCC destruction zone.

The Miaoan Au-polymetallic deposit is located in the northern TM and is a medium-sized deposit in the western part of the NCC destruction zone. Detailed geological surveys have been carried out in recent years. The orebodies occur in the Proterozoic dolomite strata surrounding the Mesozoic Laiyuan complex intrusion, which can be divided into the Xiaolinggen, Pinggou, and Niulan ore blocks. The deposit has total ore reserves of ~3.90 Mt and total metal reserves of ~5.0 t Au, ~40 t Ag, ~22,000 t Cu, and ~2000 t Zn. The average grades are ~9.3 g/t of Au, ~51.0 g/t of Ag, ~0.66% of Cu, and ~3.27% of Zn. Based on detailed field exploration work, this paper summarizes the detailed geological characteristics of the Miaoan Au-polymetallic deposit and further analyzes trace elements and S-C-O isotopic compositions of pyrite and calcite for the first time, aiming to constrain the sources of ore-forming materials and the genesis of this deposit. This is of great significance to further mineral exploration in the northern TM.

2. Regional Geology

The Miaoan Au-polymetallic deposit is located in the western part of the NCC destruction zone. The NCC, one of the oldest cratons in the world, is surrounded by the Central Asian orogenic belt to the north and the Qinling–Dabie–Sulu orogenic belt to the south (Figure 1a). It has experienced several stages of tectonic evolution from the Precambrian to the Cenozoic [28–31]. The NCC was severely destroyed in the late Mesozoic, with a destruction peak of ~125 Ma [32]. The lithosphere is strongly thinned, accompanied by extensive magmatic activity and large-scale mineralization [2,33,34]. A lot of studies have focused on the destruction of the NCC and its relationship with mineralization [1,2,35–39].

The Laiyuan complex intrusion, consisting of the Dahenan, Dahaituo, Sigezhuang, and Wang'anzhen plutons, was mainly formed in the northern TM, belonging to a part of magmatic activity induced by the destruction of the NCC. The lithology of the Laiyuan complex intrusion includes gabbro, diorite, quartz monzonite, biotite granite, granodiorite, quartz diorite, and syenite porphyry. From the early to late stage, the lithology of the Laiyuan complex intrusion displays an obvious lithologic change from basic to intermediate and to acidic (Figure 1b) [40–42]. Previous studies show that the rock-forming ages are from the Late Jurassic to the Early Cretaceous (142–134 Ma) [13,41,43].

The strata in the Miaoan region are mainly composed of the Archean metamorphic basement, the Proterozoic–Mesozoic caprock, and the Quaternary sediments. The Archean metamorphic basement is composed of the middle and lower strata of the Fuping Group, including the Nanying, Manshan, and Muchang formations. Its lithology is predominantly biotite plagioclase gneiss, leptite, marble, and plagioclase amphibolite. The Proterozoic caprock, including the Gaoyuzhuang Formation of the Changcheng System and the Wumishan Formation of the Jixian System, is mainly dolomite with a small amount of quartz sandstone and carbonaceous shale. The flint-bearing banded dolomite of the Gaoyuzhuang Formation is the host rock of skarn-type Fe–Cu deposits in this region. The Paleozoic strata mainly formed during the Cambrian–Ordovician periods, consisting of limestone, clastic rock, clay rock, and shale, which are the host rocks of skarn-type Cu–Zn–Mo deposits. The Mesozoic strata are mainly the Jurassic Tiaojishan Formation, and its predominant lithology is pyroclastic rock, molten tuff, and andesite. The Quaternary sediments are mainly alluvial and slope sediments. The fault structure is developed in this region. The regional NNE-trending Shanghuangqi–Wulonggou deep-large fault is the dominant fault, which is overlapped by the NW-trending and NE-trending faults. These faults control the attitude of Au and nonferrous metal deposits.

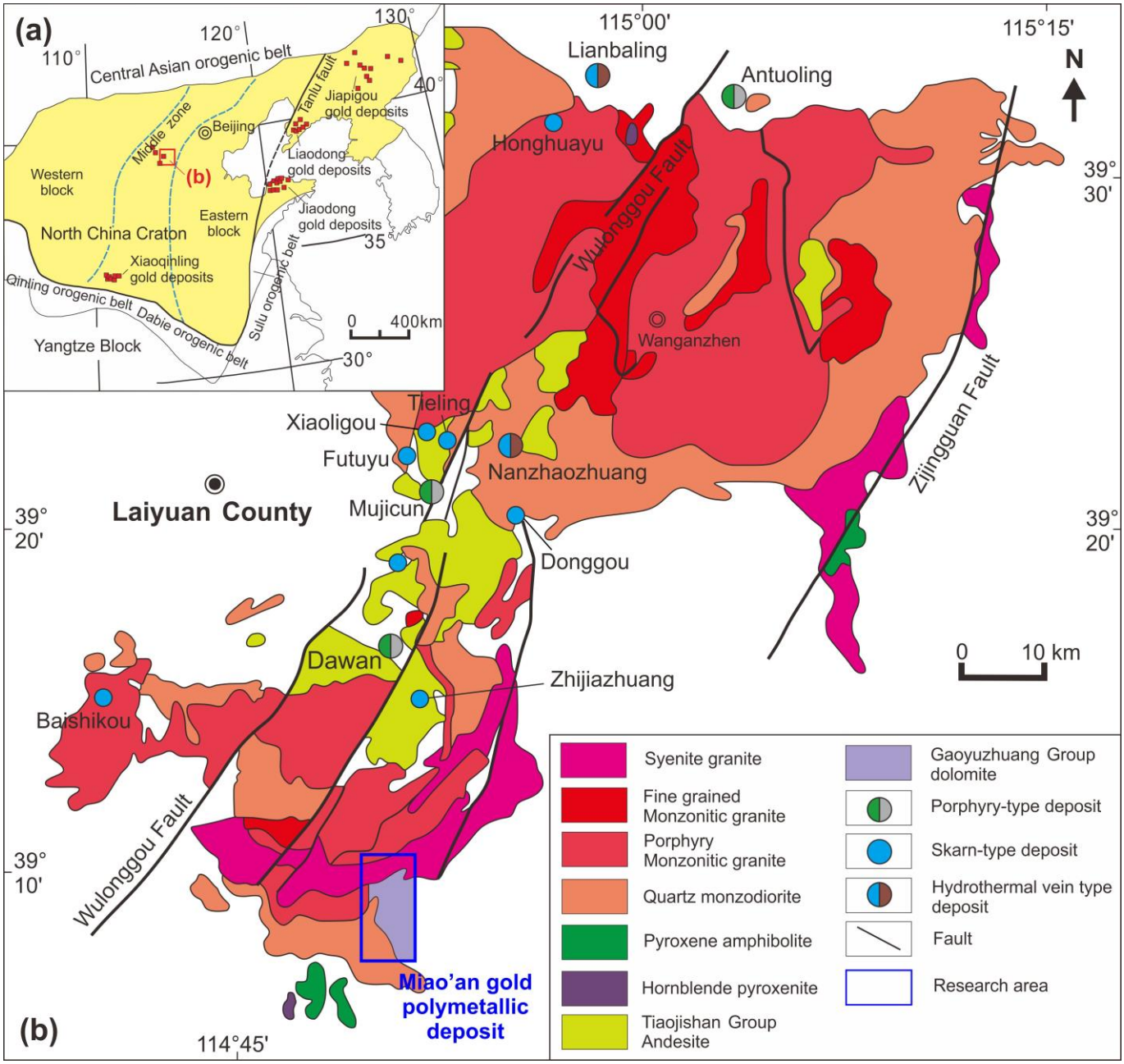

Figure 1. (**a**) Geological map of the North China Craton (modified after [2]); (**b**) simplified geological map of the northern Taihang Mountains (modified after [44]).

3. Characteristics of Ore Deposits

The exposed strata in the Miaoan area are mainly the Gaoyuzhuang Formation of the Mesoproterozoic Changcheng system, a small amount of the Muchang Formation of the Archean Fuping Group, and the Quaternary strata (Figure 2). The main lithologies of the Gaoyuzhuang Formation are dolomite and carbonaceous silty shale, which are widely distributed in the western and southeastern parts of the mining area. These strata experienced strong fold deformation and mineralization alteration, and the intersection of the fold core and the NW-trending fault is the favorable ore-hosting site for the Au orebody. The Muchang Formation is mainly gneiss. The fault structure in the mining area can be classified into three groups: NW-, NE-, and near SN-trending. The NW-trending faults are characterized by multistage activity and are commonly filled by diabase, which are the

main ore-controlling faults of Au orebodies. Intermediate-acid magmatic rocks, such as quartz monzonite, granodiorite, and granite, are developed in the mining area.

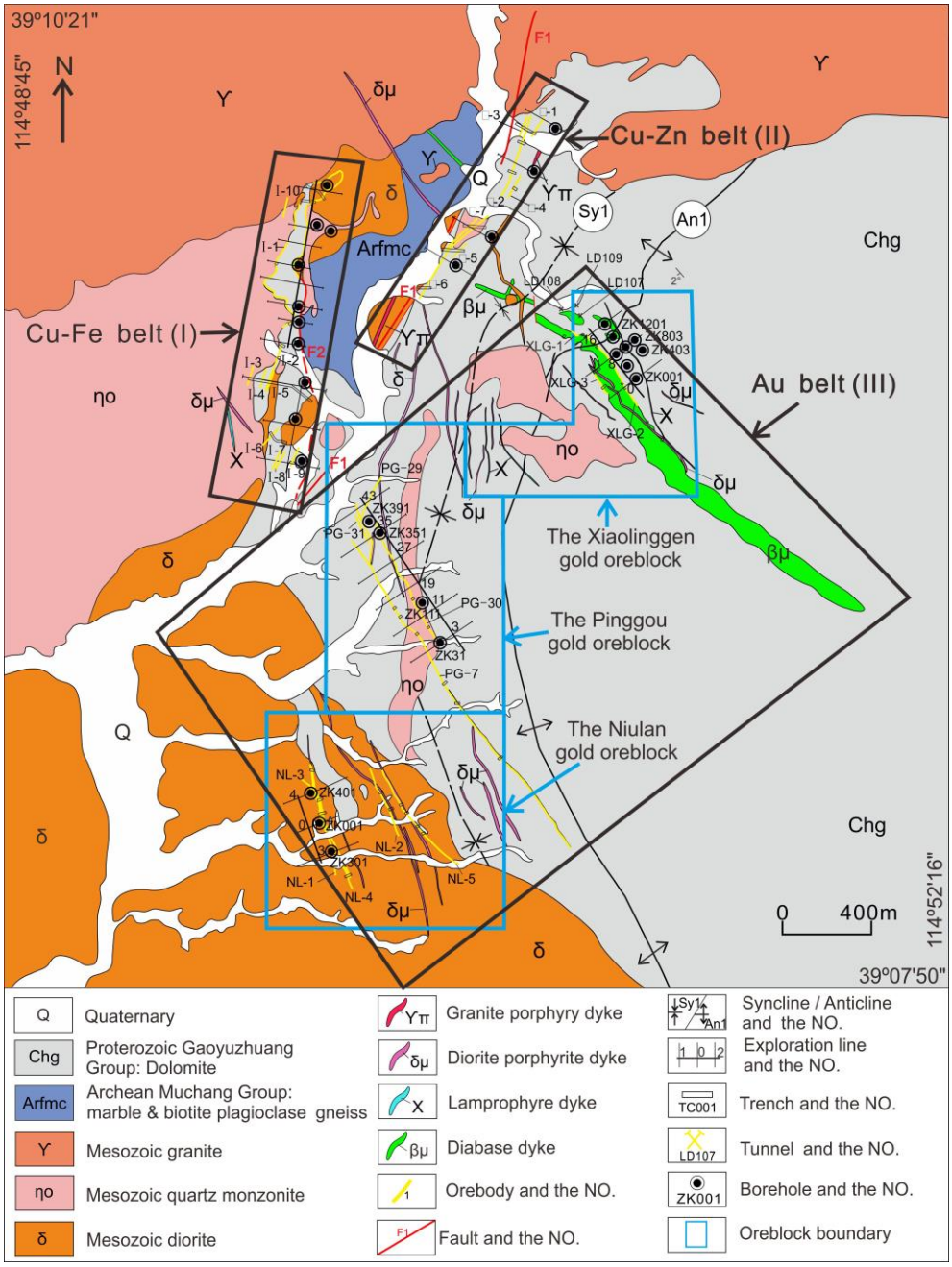

Figure 2. Geological map of the Miaoan Au-polymetallic deposit.

3.1. Orebody Characteristics

The Miaoan Au-polymetallic deposit is composed of several orebodies with different ore types. Based on the type and combination of ores, the deposit can be divided into three ore belts: (I) the Cu–Fe ore belt, (II) the Cu–Zn ore belt, and (III) the Au ore belt.

3.1.1. The Cu–Fe Ore Belt

The Cu–Fe ore belt is developed in the skarn contact zone between intermediate-acid magmatic rocks (granite, quartz monzonite, and diorite) and dolomite of the Gaoyuzhuang Formation in the northwestern part of the mining area. The length of the belt controlled by the project is ~1500 m, and the width is 100–300 m. A total of 12 orebodies have been

found in this belt, with 70°–90° dips and 60°–75° dip angles. The I-1 orebody is the largest orebody (Figure 3).

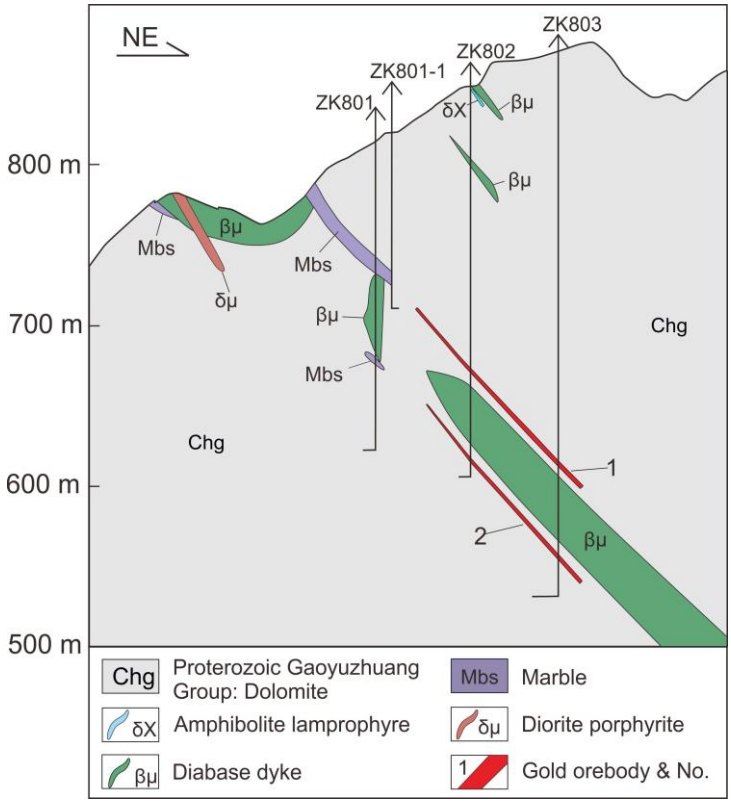

Figure 3. Section map of the No. 8 exploration line in the Xiaolinggen ore block of the Miaoan Au-polymetallic deposit.

The I-1 orebody is located in the northern section of the Cu–Fe ore belt and has a total length of ~800 m. The orebody attitude is the same as that of this ore belt. It is stratiform and saddle in shape and exhibits expansion, contraction, and pinch-out reappearance along the strike and dip. The inclination depth of the orebody is generally 80–120 m, and the maximum depth is 160 m. The maximum burial depth of the ore-bearing elevation is 559–692 m. The thickness of the orebody is generally 1.02–6.80 m, and the average thickness is 4.73 m. The orebody is generally associated with Au and Ag, with resources of 1.6 t and 28.65 t, respectively. The grades of Au and Ag can reach 17.35 g/t and 62.00 g/t, respectively.

3.1.2. The Cu–Zn Ore Belt

The Cu–Zn ore belt is located in the marble dolomite and hornfels shale of the Gaoyuzhuang Formation in the northern part of the mining area. Skarnization is developed in this belt. The ore belt is ~2000 m in length and 50–300 m in width and has an ore belt strike of 20°–30°. Seven Cu–Zn orebodies are developed in the belt, all of which are controlled by NE-trending faults. Among these, the II-2, II-4, and II-6 orebodies are large.

The II-2 orebody is located in the northern section of the Cu–Zn ore belt, with a length of 420 m and a thickness of 1.00–1.46 m. It has veined shapes and occurs in the fractured alteration zone among dolomite layers. It is characterized by expansion, contraction, and pinch-out reappearance along the strike and dip. The attitude of the orebody is 115°–135°∠56°–71°, consistent with NE-trending faults. The orebody composition follows the change rule of Cu → Cu–Zn → Zn from south to north along the strike, with Cu grades of 0.26%–0.34% and Zn grades of 0.52%–3.62%.

The II-4 orebody is located in the middle of the Cu–Zn ore belt, with a length of 100 m and thickness of ~1.00 m. The attitude of the orebody is 125°∠75°. The orebody is composed of Cu, Au, and Ag, with grades of 0.43%, 16.35 g/t, and 51.00 g/t, respectively.

The II-6 orebody is located in the southern parts of the Cu–Zn ore belt, with a length of 500 m and thickness of 1.40–2.50 m. It is vein-like along the NE-trending fault, with an orebody attitude of 102°–135°∠45°–65°. The primary components are Cu, Au, and Ag, with grades of 0.20%–3.2%, 0.22–0.32 g/t, and 8.54–17.93 g/t, respectively.

3.1.3. The Au Ore Belt

The Au ore belt is located in the central and eastern parts of the Miaoan mining area, outside of the Cu–Fe and Cu–Zn ore belts. It is controlled by the NW-trending fracture zone and is divided into three ore blocks: Xiaolinggen, Pinggou, and Niulan.

The Xiaolinggen ore block is located in the eastern part of the mining area. The mineralized zone is strictly controlled by the NW-trending fault, with a strike of ~310°, a dip of 40°–50°, a dip angle of 40°–65°, and a thickness of 1.00–8.00 m with an average of 3.00 m. It is composed of phlogopitized diabase and pyritized marble. The length of the altered mineralization zone exceeds 2600 m, but Au mineralization is discontinuous. Three industrial orebodies have primarily formed at the intersection of the NW- and NE-trending faults (Figure 3). The XLG-1 orebody is lenticular with a strike of ~40°, a dip angle of ~55°, a length of 29 m, and an average thickness of 0.79 m. The Au grade is 18.30 g/t. The XLG-2 orebody is pod-like and has expansion and contraction characteristics, with an overall strike of 315°–320°, a dip angle of 41°–66°, NE-trending dip, a length of 434 m on the surface, a thickness of 0.20–3.20 m, and an average thickness of ~1.35 m. The Au grade is 32.10 g/t. The XLG-3 orebody is NW-trending, with a dip angle of ~57°, a length of ~110 m, burial depth of ~65 m, an average thickness of ~0.84 m, and an Au grade of 6.05 g/t.

The Pinggou ore block is located in the southeastern part of the mining area. The altered mineralization zone trends NNW, with lengths greater than 2300 m and widths of ~150 m. Four Au orebodies are recognized in this ore block. These orebodies are developed in the contact zone between the marble and lamprophyre dikes.

The PG-7 orebody has a control length of 2100 m and a thickness of 0.30–0.80 m. The elements of attitude are 55°–65°∠75°–85° and the Au grade is 8.45–12.88 g/t. The PG-29 orebody has a control length of 130–180 m and a thickness of 0.40–0.49 m. The elements of attitude are 50°–65°∠70°–80° and the Au grade is 14.86–15.10 g/t. The PG-30 orebody has a control length of 150–450 m, an average thickness of 0.72 m, elements of attitude of 65°∠75°–85°, and an average Au grade of 15.97 g/t. The PG-31 orebody has a control length of ~120 m, an average thickness of 0.44 m, elements of attitude are 100°–115°∠70°–75°, and an average Au grade of 12.48 g/t.

The Niulan ore block is located in the southern part of the mining area. The orebodies, mainly structurally altered rock and quartz veins, occur in the diorite intrusion and the contact zone between dolomite and diorite. They are veined and strictly controlled by NNW-trending faults. The wallrock alteration is primarily characterized by silicification, K-feldspathization, sericitization, chloritization, and kaolinization. This ore block mainly developed three altered mineralization zones and five Au orebodies.

The NL-1 orebody has a control length of 113 m and an average thickness of 0.33 m. It inclines to the SW trend with a dip angle of 68°. It displays irregular veins and occurs in the diorite intrusion, and the average Au grade is 2.25 g/t. The NL-2 orebody has a control length of 318 m and an average thickness of 0.41 m. It inclines to the SW trend and the dip angle is 62°–85°. It displays irregular and lenticular veins and occurs in the contact zone between the diorite intrusion and lamprophyre dyke. The average grade of Au is 2.25 g/t. The NL-3 orebody has a control length of 591 m and an average thickness of 0.27 m. It inclines to the SW trend and the dip angle is 70°–87°. It occurs in the contact zone between the diorite dike and the lamprophyre vein. Along the strike and dip, it has wavy fluctuation, expansion and contraction, and branch compounding characteristics.

The average Au grade is 15.37 g/t. The NL-4 orebody has a control length of 333 m and an average thickness of 0.28 m. It inclines to the SW trend, and the dip angle is 72°–82°. It displays irregular veins and occurs in the diorite intrusion, with an average Au grade of 3.62 g/t. The NL-5 orebody has a control length of 606 m and an average thickness of 0.33 m. It inclines to the SW trend, and the dip angle is 73°–85°. It displays irregular and lenticular veins and occurs in the contact zone between the diorite dike and the lamprophyre vein. The average Au grade is 13.49 g/t.

3.2. Ore Characteristics

3.2.1. Ore Type

The Cu–Fe ores are located in the skarn zone between the intermediate-acid intrusion and dolomite wallrock. The skarn-type Cu–Zn ores with a small amount of hydrothermal veins mainly occur in dolomite, which is far from the intrusion. The Au ores occur in the fracture zone in the periphery of the intrusion, dominated by quartz-sericite-pyrite altered rock and quartz vein types (Figure 4).

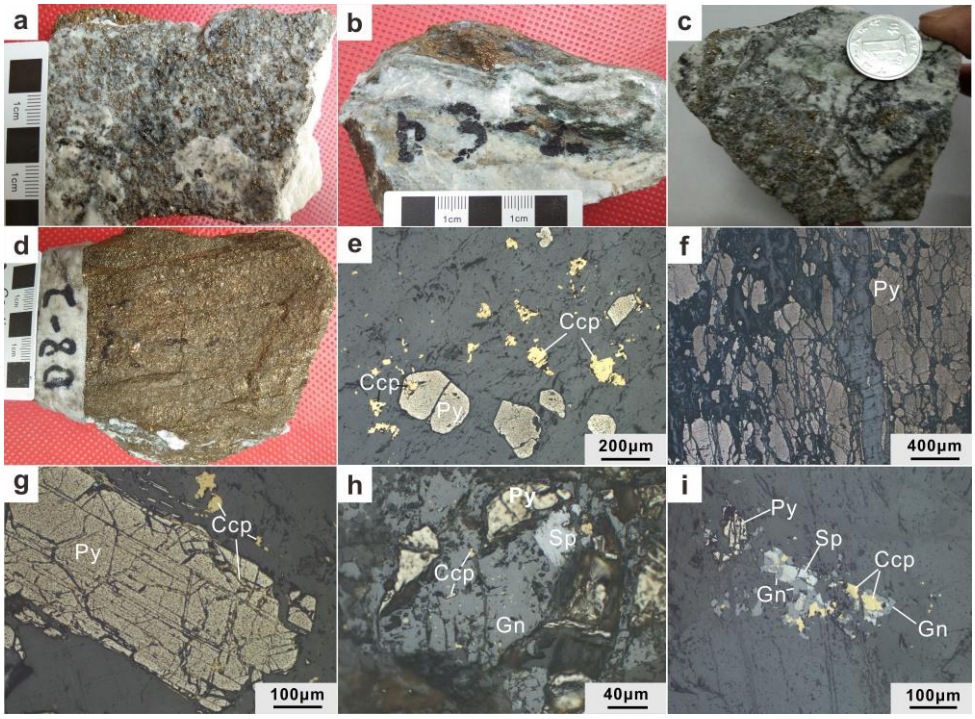

Figure 4. The mineralization characteristics of the Miaoan Au-polymetallic deposit. (**a**–**c**) Pyrite in marble; (**d**) massive pyrite; (**e**) symbiosis of euhedral pyrite and chalcopyrite; (**f**) pyrite is closely associated with carbonate veins; (**g**) pyrite is euhedral and cataclastic, and chalcopyrite is filled along pyrite fractures; (**h**) symbiosis of pyrite with galena and sphalerite; chalcopyrite exsolution in galena in the form of a milk drop; (**i**) symbiosis of pyrite with chalcopyrite, galena, and sphalerite. Py: Pyrite; Ccp: Chalcopyrite; Gn: Galena; Sp: Sphalerite.

3.2.2. Mineral Composition, Texture, and Structure

The skarn-type ores are predominantly composed of magnetite, chalcopyrite, sphalerite, pyrite, pyrrhotite, and chalcocite. The ores are mainly subhedral-anhedral granular, replacement, and poikilitic textures and are dominated by massive and banded structures, followed by disseminated and taxitic structures. For the hydrothermal vein-type ores, the ore minerals are mainly pyrite, followed by magnetite, ilmenite, chalcopyrite, and molybdenite. The ores mainly have granular, colloidal, and crystalloblastic textures and have disseminated and honeycombed structures, followed by veined and filling structures. Gold occurs in the fissure and intercrystalline of pyrite or the cavity of limonite. The gold grade is positively correlated with ore minerals, especially fine pyrite.

3.2.3. Wall-Rock Alteration

The Miaoan deposit has extensive and intense wallrock alteration, and the main types are skarnization, silicification, beresitization, chloritization, and carbonatation. Skarnization develops along the contact zone between intermediate-acid magmatic rocks and the dolomite strata, which is usually located at the edge of the mineralized alteration zone and is the main mineralization type of Cu–Fe and Cu–Zn ores. Silicification is the main symbol of hydrothermal alteration, which is developed in the central part of the mineralization alteration zone. It is formed by the filling of siliceous-rich hydrothermal fluid in the fault zone or fracture and is closely related to Au mineralization. Beresitization is mostly developed in the central part of the mineralized alteration zone, superimposed with extensive sericitization. It is mainly composed of pyrite, sericite, and quartz, accompanied by polymetallic sulfide mineralization. Chloritization is primarily developed in the outermost Au ore belt along the contact zone of the diabase vein and the intermediate-acid rock, and the nearby fracture surfaces. Carbonation developed on both sides of the fault zone and in the fissures, often in the form of veinlets or reticulate veins. The altered minerals are mainly calcite, which is the product of low-temperature alteration in the mineralization stage.

4. Samples and Methods

Pyrite samples for Rb-Sr isotopic dating, trace element and sulfur isotopic analyses, and calcite samples for C–O isotopic composition analyses were collected from the Xiaolinggen ore block in the Miaoan Au-polymetallic deposit (Figures 2 and 3). Sample preprocessing and mineral separation were conducted in the Hebei Regional Geological Survey and Research Institute laboratory. The pyrite and calcite grains were selected under a binocular microscope. Then, they were crushed to 200 mesh without pollution.

4.1. Pyrite Rb-Sr Isotopic Dating

Rb and Sr cannot enter pyrite in large quantities. However, trace element abundances in pyrites show relatively high levels of Rb, Sr, and rare earth elements, which may reside in inclusions or crystal defects [45]. With the development of analytical technology, numerous studies have shown that there are sufficient amounts of Rb and radiogenic Sr contents and variable Rb/Sr ratios in pyrite for Rb-Sr isotopic dating [46,47]. Therefore, pyrite Rb-Sr isotopic dating is widely used in determining the age of mineralization [48–51]. In this study, pyrite samples were first crushed to 40–60 mesh, and then fresh and high-purity particles were selected under binoculars. The Rb and Sr concentrations and isotopic composition of pyrite were determined at the Technical Service Center, Institute of Soil Science, Chinese Academy of Sciences. The pyrite samples were washed with deionized water, dried at low temperature, and then ground to 200 mesh in an agate mortar. The 200-mesh powder was digested with a mixed acid to form a clear solution, and it was left to stand for 12 h. The solution was divided into two parts, which were used to determine the isotope ratio (without spikes) and the isotope content (with spikes). The elements were separated by ion exchange columns, and isotopic determination was performed using VG354 multicollector mass spectrometry manufactured by British VG Company. A reference standard of NBS987 = 0.710241 $\pm$ 7 (2σ) was used for monitoring the data quality. The whole produce blank of Sr is 3 ng. The $^{87}Sr/^{86}Sr$ ratios were normalized to $^{86}Sr/^{88}Sr$ = 0.1194 to correct for instrument fractionation. The isochron age was calculated using the ISOPLOT program [52]. A more detailed analytical process can be found in a previous study [53].

4.2. Trace Element and S-C-O Isotopic Composition Analyses

All analyses were conducted at the Analysis and Test Center of the Beijing Institute of Geology of Nuclear Industry. The pyrite trace elements were determined using a Thermo Fisher ELEMENT XR inductively coupled plasma mass spectrometer (ICP-MS). The analytical accuracy is better than 5% when the element content is more than 10^{-6}, and

the analytical accuracy is better than 10% when the element content is less than 10^{-6}. The detailed analytical process can be found in Chen, et al. [54] and Guo, et al. [55].

The S isotopes of pyrites were determined using a Finnigan MAT-251 gas isotope mass spectrometer. The analytical results are described relative to V-CDT, and the analytical accuracy is better than ±0.2%. The detailed analytical process can be found in Li, et al. [56]. The C–O isotopes of calcites were determined using a Finnigan MAT-253 gas isotope mass spectrometer. The C isotopic values are reported relative to the Pee Dee Belemnite standard (V-PDB). The reference standards of the O isotopic values are V-PDB and Vienna Standard Mean Ocean Water (V-SMOW). The analytical accuracy is better than ±0.2%. The detailed analytical process is described in Xue, et al. [57].

5. Results

5.1. Pyrite Rb-Sr Isochron Age

Pyrite is the most important gold-bearing mineral and has a close genetic relationship with gold mineralization. It is an important means of obtaining the age of gold mineralization. Four valid pyrite Rb-Sr isotope dating samples were obtained, and the results are summarized in Table 1. The Rb and Sr concentrations of the pyrite samples range from 0.2952 to 0.8907 ppm and from 0.6592 to 7.586 ppm, respectively. The $^{87}Rb/^{86}Sr$ ratios range from 0.1176 to 3.981, and the $^{87}Sr/^{86}Sr$ ratios range from 0.712953 to 0.720021. Four samples are plotted in Figure 5, and a straight line is fitted through the least square method, which defines a robust isochron age of 129.5 ± 2.5 Ma (MSWD = 1.6) with an initial $^{87}Sr/^{86}Sr$ value of 0.712685 ± 0.000078 (Figure 5). This age can represent the mineralization age.

Table 1. Rb-Sr isotopic compositions of pyrites from the Miaoan Au-polymetallic deposit.

Pyrite	Rb (ppm)	Sr (ppm)	$^{87}Rb/^{87}Sr$	$^{87}Sr/^{86}Sr$	2σ
D6-1	0.3018	7.586	0.1176	0.712953	0.00005
D8-1	0.8907	0.6592	3.981	0.720021	0.00005
D9-1	0.5623	1.093	1.527	0.715513	0.00005
D11-1	0.2952	0.9964	0.8732	0.714215	0.00005

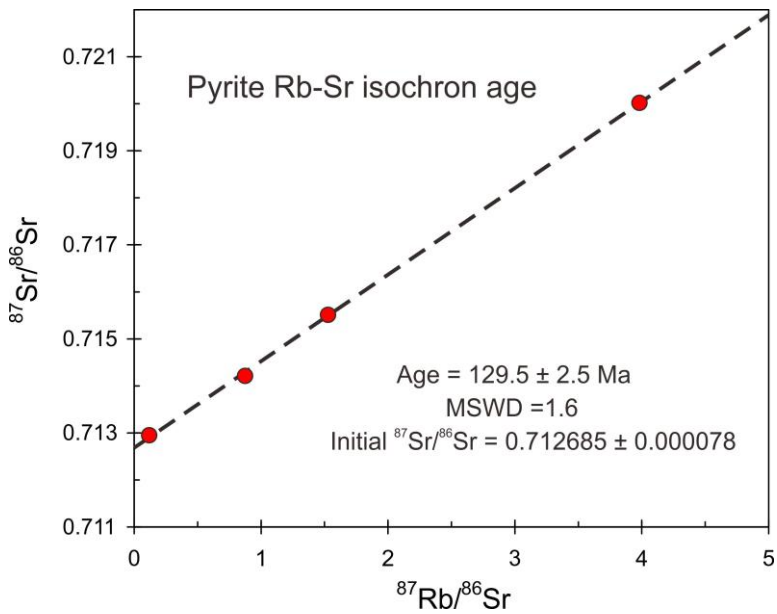

Figure 5. Pyrite Rb-Sr isochron age for the Miaoan Au-polymetallic deposit.

5.2. Trace Element Compositions of Pyrites

The trace element compositions of the pyrites from the Miaoan Au-polymetallic deposit are listed in Table 2. The REE contents in pyrites are 0.36–8.60 ppm, with an average of 3.45 ppm.

They show right-inclined chondrite-normalized REE patterns (LREE/HREE = 4.86–18.64; $(La/Yb)_N$ = 7.77–35.38) with obviously negative Eu anomalies ($\delta Eu = Eu_N/(Sm_N * Gd_N)^{1/2}$ is 0.18–0.94, where the subscript N represents chondrite normalization) (Figure 6). The contents of siderophile and chalcophile in pyrites have a large variation range, with Co contents of 24.5–4093 ppm, Ni contents of 2.23–343 ppm, Cu contents of 24.2–287 ppm, Pb contents of 8.14–1402 ppm, and Zn contents of 18.1–247 ppm. High field strength elements also have a large variation range, with Nb contents of 0.009–0.21 ppm, Ta contents of 0.002–0.048 ppm, Zr contents of 0.29–3.40 ppm, and Hf contents of 0.003–0.069 ppm. Correspondingly, these pyrites show high Y/Ho ratios of 24.6–34.4 and Co/Ni ratios of 1.50–23.39 (Figure 7). In addition, Hf/Sm ratios of 0.029–1.59, Nb/La ratios of 0.011–0.81, Th/La ratios of 0.027–2.04, Zr/Hf ratios of 19.4–243, and Nb/Ta ratios of 4.38–70.0 show a large variation range.

Table 2. Trace element compositions (ppm) of pyrites from the Miaoan Au-polymetallic deposit.

	D6-1	D7-1	D9-2	D10-1	D14-2	D16-1	D17-2
La	0.88	0.66	1.06	0.24	2.17	0.077	0.26
Ce	1.55	1.32	2.50	0.59	4.18	0.16	0.37
Pr	0.16	0.14	0.31	0.086	0.40	0.013	0.042
Nd	0.68	0.45	1.66	0.45	1.25	0.051	0.17
Sm	0.074	0.073	0.31	0.084	0.14	0.012	0.037
Eu	0.014	0.010	0.019	0.004	0.037	0.004	0.010
Gd	0.077	0.054	0.20	0.042	0.17	0.014	0.052
Tb	0.008	0.008	0.025	0.005	0.016	0.002	0.008
Dy	0.035	0.041	0.10	0.022	0.098	0.011	0.044
Ho	0.006	0.007	0.009	0.003	0.019	0.003	0.013
Er	0.024	0.018	0.029	0.013	0.061	0.007	0.035
Tm	0.004	0.002	0.003	0.002	0.007	0.002	0.004
Yb	0.024	0.016	0.023	0.008	0.044	0.006	0.024
Lu	0.002	0.003	0.002	0.002	0.005	0.002	0.003
Y	0.20	0.21	0.31	0.099	0.49	0.083	0.32
∑REE	3.54	2.8	6.25	1.55	8.60	0.36	1.07
LREE/HREE	18.6	17.8	15.0	15.0	19.5	6.74	4.86
$(La/Yb)_N$	26.2	29.5	33.1	21.5	35.4	9.21	7.77
δEu	0.56	0.47	0.22	0.18	0.73	0.94	0.70
δCe	0.94	1.02	1.06	1.01	1.02	1.13	0.79
Co	2034	1360	24.5	56.4	4093	514	1066
Ni	151	218	2.23	3.86	175	343	171
Cu	128	125	24.2	57.8	246	148	287
Pb	139	304	238	229	8.14	688	1402
Zn	193	216	154	247	18.1	149	26.9
Nb	0.020	0.014	0.012	0.009	0.14	0.015	0.21
Ta	0.002	0.002	0.002	0.002	0.002	0.002	0.048
Th	0.024	0.078	0.050	0.11	0.13	0.033	0.53
Zr	0.31	0.38	0.45	0.29	2.37	3.40	1.72
Hf	0.016	0.016	0.009	0.003	0.069	0.014	0.059
Li	5.46	5.33	8.19	7.21	5.67	5.17	5.63
Sc	0.28	0.17	0.15	0.13	0.93	0.49	0.38
V	9.08	0.82	2.12	1.99	3.27	2.64	5.90
Cr	1.29	0.71	0.92	0.99	1.99	0.78	1.54
Mo	3.47	2.79	0.29	0.39	7.22	1.27	1.12
W	0.30	0.24	0.18	0.13	0.25	0.13	10.10
Cd	0.82	0.87	0.39	0.75	0.048	0.49	0.12
Tl	0.13	0.14	0.017	0.064	0.22	0.13	0.088
U	0.035	0.032	0.013	0.12	2.77	0.044	0.16
Sr	2.19	2.31	2.26	1.44	2.68	2.02	1.52
Ba	2.86	2.48	0.10	1.73	5.14	2.17	2.70
Co/Ni	13.47	6.24	10.99	14.61	23.39	1.50	6.23
Hf/Sm	0.22	0.22	0.029	0.036	0.50	1.17	1.59

Table 2. *Cont.*

	D6-1	D7-1	D9-2	D10-1	D14-2	D16-1	D17-2
Nb/La	0.023	0.021	0.011	0.038	0.065	0.19	0.81
Th/La	0.027	0.12	0.047	0.46	0.060	0.43	2.04
Y/Ho	33.3	30.0	34.4	33.0	25.8	27.7	24.6
Zr/Hf	19.4	23.8	50.0	96.7	34.4	242.9	29.2
Nb/Ta	10.00	7.00	6.00	4.50	70.00	7.50	4.38

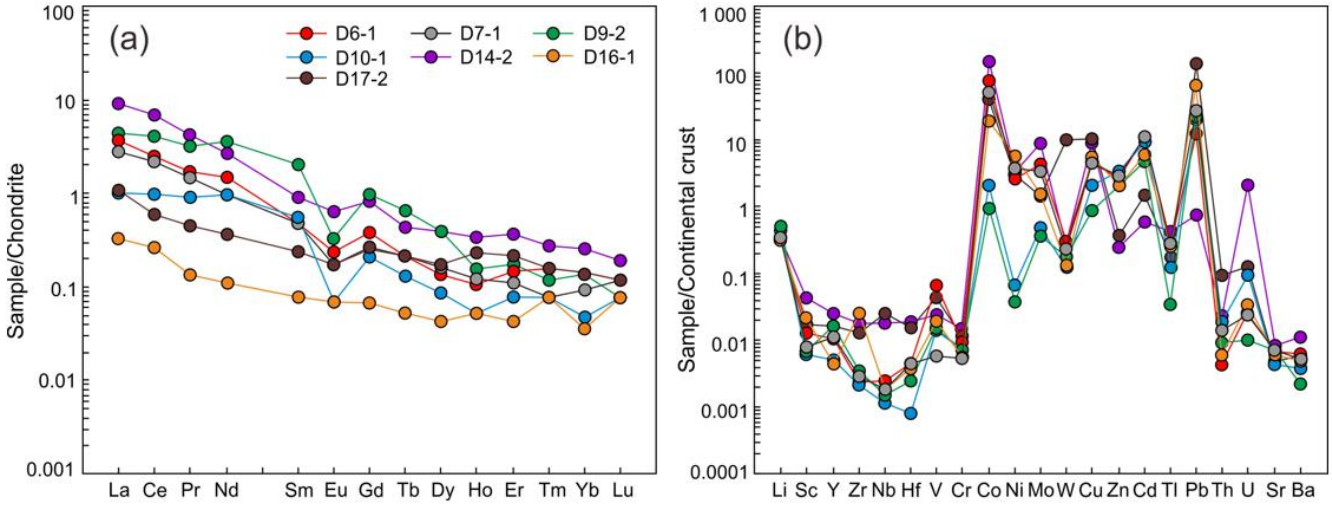

Figure 6. (**a**) Chondrite-normalized rare earth element patterns of ores (normalization values from reference [58]); (**b**) continental crust-normalized trace element spider diagram of ores (normalization values from reference [59]).

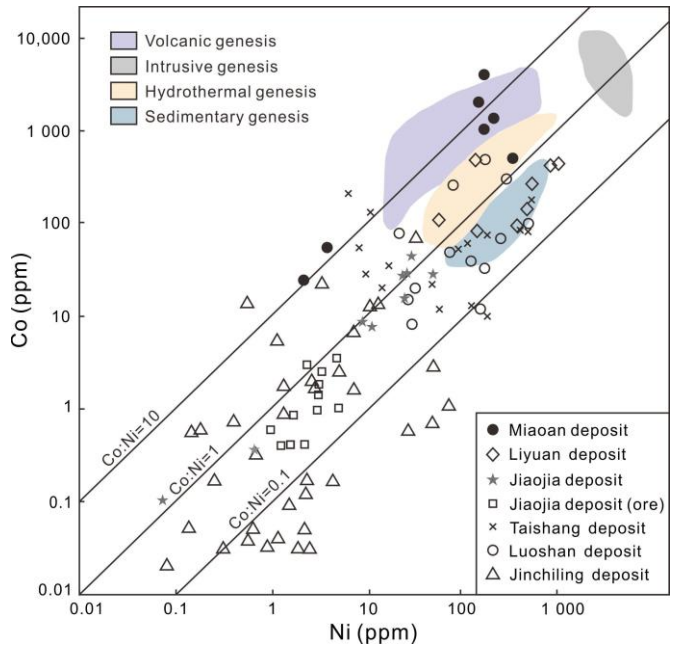

Figure 7. Co-Ni distribution diagram of pyrites from the Miaoan Au-polymetallic deposit and other typical gold deposits in the Jiaodong and Taihang regions (modified after references [60,61]).

5.3. Sulfur Isotopic Composition of Pyrite

The sulfur isotopic compositions of nine pyrites from the ores in the Miaoan Au-polymetallic deposit are listed in Table 3 and plotted in Figure 8. Most $\delta^{34}S$ values range from −2.0‰ to 1.6‰, except for samples D11-1 and D14-2, which are −5.5‰ and −5.0‰,

respectively. The S isotopic compositions of the Au and Cu deposits in the northern TM determined by previous studies are also displayed in Figure 8. The $\delta^{34}S$ values of the Shihu Au deposit range from −2.2‰ to 3.0‰ [13,62,63], the Yixingzhai Au deposit from −0.3‰ to 3.6‰ [24], and the Mujicun Cu–Mo deposit from −3.5‰ to 4.3‰ [64–66]. The $\delta^{34}S$ values of pyrite, chalcopyrite, and sphalerite in the Liyuan Au deposit range from 0.9‰–4.3‰, and those of galena range from −12.8‰ to 1.4‰ [67]. Thus, the S isotopes of these polymetallic deposits in the northern TM have a large range, but most values are concentrated in a narrow range of −1‰ to 4‰ (Figure 8). These results possibly mean that the ore-forming fluids mainly originated from magma but involved other fluids.

Table 3. Sulfur isotopic compositions of pyrites from the Miaoan Au-polymetallic deposit.

Sample No.	Ore Type	Minerals	$\delta^{34}S_{V\text{-}CDT}$ (‰)
D6-1	Hydrothermal vein type	Pyrite	1.3
D7-1			0.9
D8-1			1.6
D9-2			−0.6
D10-1			−1.5
D16-1			−2.0
D17-1			−1.1
D11-1			−5.5
D14-2			−5.0

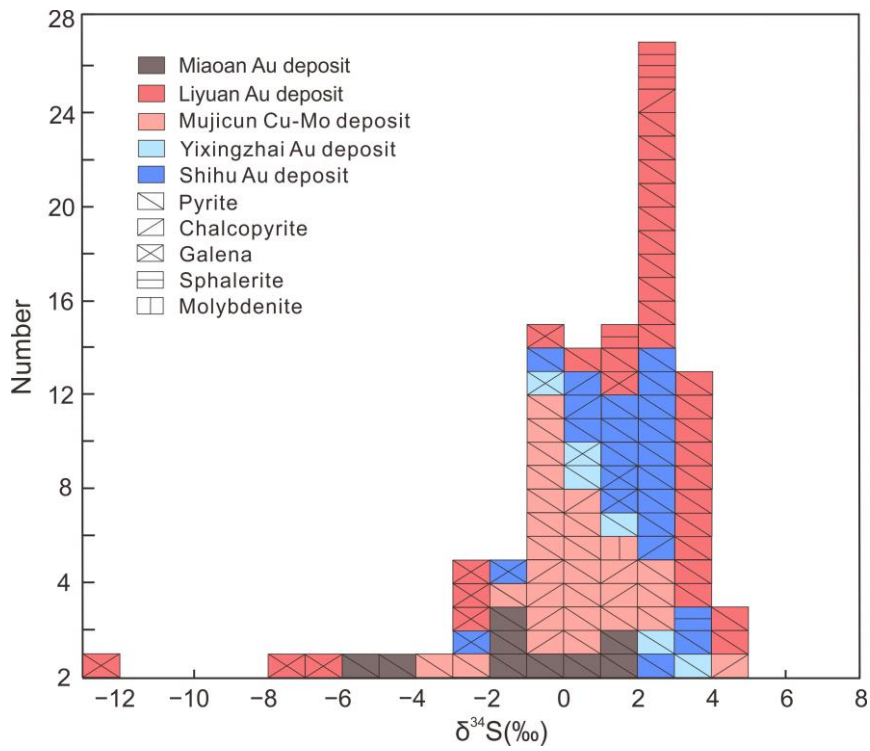

Figure 8. Histogram of S isotope data for gold and nonferrous metal deposits in the northern Taihang Mountain. The data of this histogram are sourced from this study and the literature (the Miaoan Au-polymetallic deposit (this study), the Mujicun Cu deposit [64–66], the Shihu gold deposit [13,62,63], the Yixingzhai gold deposit [24], and the Liyuan gold deposit [67]).

5.4. Carbon and Oxygen Isotopic Compositions of Calcite and Ore

The results of the C–O isotopic compositions of hydrothermal calcites and ores in the Miaoan Au-polymetallic deposit are shown in Table 4 and plotted in Figure 9. The $\delta^{13}C_{V\text{-}PDB}$ values of the calcite and ore samples ranged from −4.2‰ to −2.0‰ and −6.3‰ to −2.5‰, respectively. Relative to the V-PDB standard, the $\delta^{18}O_{V\text{-}PDB}$ values of calcite and ore varied

from −21.0‰ to −15.0‰ and −20.1‰ to −12.9‰, respectively. For the V-SMOW, the $\delta^{18}O_{V\text{-}SMOW}$ values of calcite and ore varied from 9.3‰ to 15.4‰ and 9.3‰ to 17.6‰, respectively. The results show that ore and calcite have similar C–O isotope compositions. They lie in the field between magmatic rocks and marine carbonates, suggesting multiple sources of ore-forming fluids.

Table 4. Carbon and oxygen isotopic compositions of calcites and ores from the Miaoan Au-polymetallic deposit.

Sample No.	Mineral	$\delta^{13}C_{V\text{-}PDB}$(‰)	$\delta^{18}O_{V\text{-}PDB}$(‰)	$\delta^{18}O_{V\text{-}SMOW}$(‰)
D6-1	calcite	−3.9	−16.7	13.7
D11-1		−2.8	−18.1	12.3
D14-2		−2.9	−15.0	15.4
D16-1		−4.2	−21.0	9.3
D17-1		−2.0	−18.5	11.9
D6-2	ore	−6.3	−20.9	9.3
D8-2		−4.6	−12.9	17.6
D9-1		−2.8	−20.1	10.1
D10-2		−3.0	−19.5	10.8
D11-2		−2.5	−16.0	14.4

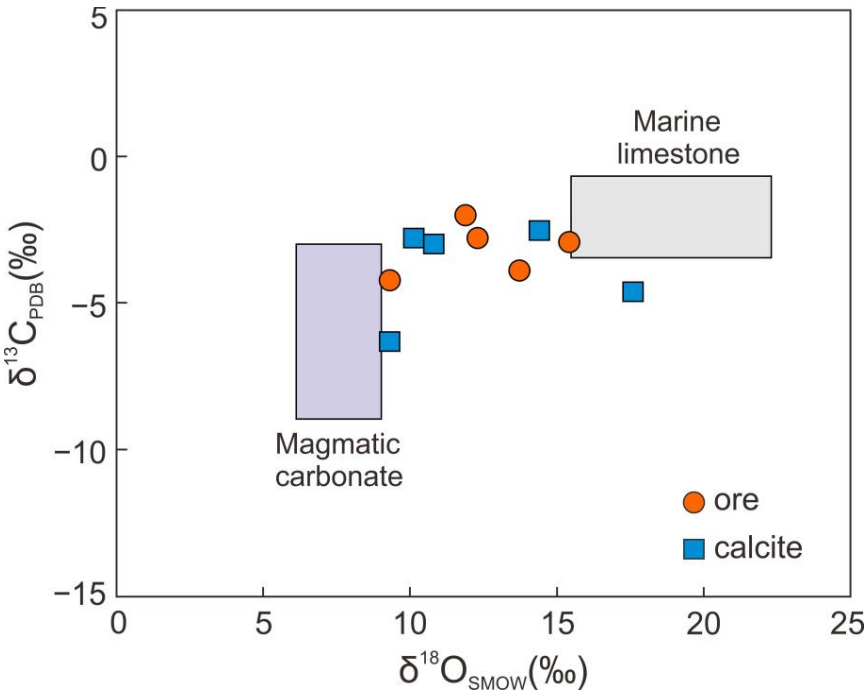

Figure 9. $\delta^{13}C$-$\delta^{18}O$ diagram of the Miaoan Au-polymetallic deposit.

6. Discussion

6.1. Geochronology

A robust ore-forming age is critical to understanding petrogenesis and tectonic settings. In this study, pyrites from the Miaoan Au-polymetallic deposit yield an Rb-Sr isochoron age of 129.5 ± 2.5 Ma. Pyrite is the most important gold-carrying mineral, and this age constrains the time of gold mineralization. The ore-forming age is consistent with the pyrite Re–Os isochron age of the Shihu gold deposit in the southern part of the TM [68]. The Miaoan Au-polymetallic deposit is spatially close to the Laiyuan intrusion. A large number of chronological studies have been conducted previously [1,35,41,42,65,69–72]. The granitoids in the Laiyuan complex have ages of 137–128 Ma [42,72], which are close to the ore-forming age of the Miaoan Au-polymetallic deposit, suggesting their genetic relation-

ship. The magmatic activity may have provided thermo or material for the mineralization. In addition, the rock- and ore-forming ages agree well with the timing of the destruction of the NCC [2]. Mineralization may be associated with this tectonic setting.

6.2. The Properties of the Ore-Forming Fluids

Trace elements have difficulty entering the lattice of pyrite and primarily occur in the fluid inclusions or crystal defects of pyrite. Therefore, the trace elements of pyrite can reflect the characteristics of ore-forming fluids [2,56,73–77].

The pyrites in the Miaoan Au-polymetallic deposit have low REE contents (0.36–8.60 ppm) and are enriched in LREEs relative to HREEs (LREE/HREE ratios of 4.86–18.64 and La_N/Yb_N ratios of 7.77–35.38; Table 2). The REE distribution pattern of pyrite is weakly right-inclined (Figure 6), which should be due to the high Cl- or F- ions in the ore-forming fluid [78,79]. The Hf/Sm, Th/La, and Nb/La ratios were generally less than 1 in Cl-rich hydrothermal fluids and were generally greater than 1 in F-rich hydrothermal fluids. The HFSEs are commonly enriched in F-rich hydrothermal fluids [80]. The trace elements in the pyrites of the Miaoan Au-polymetallic deposit were depleted in HFSE and relatively enriched in chalcophile elements, such as Co, Cu, Zn, and Pb, and large ion lithophile elements, such as Li, Sc, Y, and Nb (Figure 6). This suggests that the ore-forming fluid has Cl-rich features. The ratios of Th/La and Nb/La were less than 1, which is also in good agreement with the Cl-rich feature for the ore-forming fluid. This is similar to those of the Jiaojia gold deposit in the Jiaodong Peninsula [56].

Co and Ni may replace Fe^{2+} in pyrite by isomorphism. Therefore, the Co/Ni ratio is significant in terms of the formation of pyrite [61]. The results show that the Co/Ni ratio of sedimentary pyrite is typically less than 1, averaging 0.63. The average Co/Ni ratio of hydrothermal pyrite is approximately 1.7, and the individual values are generally less than 5. The Co/Ni ratio of pyrite related to magmatic origin is generally greater than 5 and typically from 5 to 50 [81]. In the Miaoan Au-polymetallic deposit, the Co/Ni ratios of pyrite range from 1.50 to 23.39, with an average value of 10.92, which is consistent with those of magmatic origin. In Figure 7, the pyrite of the Miaoan Au-polymetallic deposit plots in the magmatic, hydrothermal, and lower left range, all of which are located near the line of Co/Ni = 10, with a relatively concentrated distribution. The Co and Ni contents and the Co/Ni ratios are similar to those of the Liyuan gold deposit in the center of the NCC but higher than those of the gold deposits in the Jiaodong area. Compared with that of the Jiaodong gold deposits [56], the distribution of the pyrite Co/Ni ratios of the Miaoan Au-polymetallic deposit was relatively concentrated (Figure 7), indicating that pyrite is likely related to volcanism and hydrothermal fluids.

The ratios of Y/Ho, Zr/Hf, and Nb/Ta were stable in the same hydrothermal system. However, these ratios will have a large range when hydrothermal activity is affected by metasomatism or other hydrothermal activities [82,83]. In this study, the Y/Ho values of pyrite (24.6–34.4) were similar to those of the mantle (25–30), indicating the contribution of mantle materials. The Zr/Hf and Nb/Ta ratios of pyrite in the Miaoan Au deposit vary widely (19.4–243 and 4.38–70.0). This suggests that the ore-forming hydrothermal system may have undergone strong metasomatism or been affected by external fluids.

6.3. Physicochemical Conditions of Mineralization

The pyrite in the Miaoan Au-polymetallic deposit has no obvious Ce anomalies (δCe = 0.79–1.13), but Eu shows a clear negative anomaly (δEu = 0.18–0.94). Ce and Eu are variable valence elements in REEs that are sensitive to changes in redox conditions. Under oxidizing conditions, Ce^{3+} is oxidized to Ce^{4+} and separated from the other REEs. This result demonstrates a Ce anomaly, which reflects the redox environment of the system [56]. The range of δCe variation in pyrite in the Miaoan Au-polymetallic deposit was relatively small, showing a change from a weak negative anomaly to a weak positive anomaly. This implies that the ore-forming system is in a physical and chemical environment of relative reduction. In a high-temperature reducing hydrothermal solution, Eu^{3+} is easily reduced

to Eu^{2+} and separated from the hydrothermal system to enter the mineral phase, resulting in a positive Eu anomaly in the minerals. When the corresponding system is in a low-temperature reducing environment, it easily produces negative europium anomalies in minerals [54,56]. The δEu values of the Miaoan Au-polymetallic deposit show significant negative anomalies (δEu = 0.18–0.94), indicating that the metallogenic system was a low-temperature reducing environment.

6.4. Source of Ore-Forming Fluids

The $\delta^{13}C_{V\text{-}PDB}$ values in the Miaoan Au-polymetallic deposit range from −6.3‰ to −2.0‰, with a relatively concentrated range and heavy C deficiency. The $\delta^{18}O_{V\text{-}SMOW}$ values range from 9.3‰ to 17.6‰ and have a wide range (Table 4). The C–O isotopic composition in the $\delta^{13}C$–$\delta^{18}O$ diagram was observed in the region between magmatic-origin carbonate and marine carbonate rocks (Figure 7).

The CO_2 degassing of the hydrothermal fluid had no significant effect on the O isotopic composition of the fluid, although it significantly impacted the C isotopic composition; the corresponding calcite $\delta^{13}C$ values varied over a wide range [84]. The range of the $\delta^{13}C$ values of hydrothermal calcite in the Miaoan Au-polymetallic deposit was narrow (from −6.3‰ to −2.0‰). Its genesis was unrelated to the degassing of CO_2, although it is the product of the water–rock interaction between the hydrothermal fluid and wall rock [84,85]. Previous studies have shown that the $\delta^{13}C_{V\text{-}PDB}$ values of mantle ejection and magma range from −5‰ to −2‰ and −9‰ to −3‰ [86], respectively. The $\delta^{13}C_{V\text{-}PDB}$ values of sedimentary carbonate range from −2‰ to 3‰, and the $\delta^{13}C_{V\text{-}PDB}$ values of marine carbonate are approximately 0‰ [87]. The $\delta^{13}C_{V\text{-}PDB}$ values of organic carbon in various rocks range from −30‰ to −15‰ [88]. The $\delta^{13}C_{V\text{-}PDB}$ values of the Miaoan Au-polymetallic deposit (from −6.3‰ to −2.0‰) were similar to those of mantle-derived or magmatic-origin deposits (from −5‰ to −2‰ and −9‰ to −3‰, respectively). These results are consistent with the C isotopic composition of the Early Cretaceous gold deposits in the NCC (the $\delta^{13}C_{V\text{-}PDB}$ is between −7‰ and −3‰) [2]. This interpretation is also consistent with the high-temperature C isotopic composition in granite intrusive rocks and basalts [89]. It is suggested that ore-forming hydrothermal fluid may be related to the devolatilization of magma or the degassing of the mantle during the cooling process.

There were also significant differences in the O isotopic compositions of hydrothermal fluids from different sources [90]. The $\delta^{18}O_{V\text{-}SMOW}$ value of the Miaoan Au-polymetallic deposit (9.3‰–17.6‰) was similar to that of magma or deep crustal fluid (6‰–15‰) and significantly higher than that of atmospheric precipitation, groundwater, or seawater (approximately 0‰). This indicates that the source of the ore-forming materials was closely related to magma or deep crustal fluid. According to the $\delta^{13}C$–$\delta^{18}O$ diagram (Figure 9), the ore-forming fluid should largely be from magmatic sources and contaminated by crustal materials.

The S isotopic composition of pyrite in the Miaoan Au-polymetallic deposit ($\delta^{34}S$ isotopes from −5.5‰ to 1.6‰) is generally within the range of magmatic S (from −5‰ to 5‰) [74,88,91–93]. This indicated that the ore-forming materials had characteristics of deep magmatic origin, consistent with the findings of a previous study on the western gold belt of the NCC gold metallogenic province [2]. Previous studies on the S isotopic compositions of Au–Cu (Mo) deposits in the central and northern TM regions have a small difference (Table 3) and a tower distribution (Figure 8), indicating that the main fluid sources of gold and nonferrous metal deposits in this area are similar. The $\delta^{34}S$ values of pyrite, chalcopyrite, and sphalerite were predominantly between −3.5‰ and 4.3‰ [13,24,27,62–67], displaying characteristics of deep-seated magmatic sulfur. The variation of pH or oxygen fugacity in hydrothermal systems may be responsible for the fractionation of S isotopes [27,67]. The S isotopic composition of various sulfides and sulfates crystallized from the hydrothermal system is largely dependent on temperature, pH, oxygen fugacity (fO_2), and ionic strength. Statistical analysis of the S isotopic composition of metal sulfides and sulfates in different deposits in the northern TM shows that $\delta^{34}S$ values exhibited a descending trend:

$\delta^{34}S_{pyrite} > \delta^{34}S_{sphalerite} > \delta^{34}S_{chalcopyrite} > \delta^{34}S_{galena}$ [13,24,62,64,68]. This indicates that the S isotopes in the ore-forming system have reached fractionation equilibrium, and the S isotopic composition of sulfide represents the S isotopic composition in the ore-forming fluids. In addition, the $\delta^{34}S$ values of gold and nonferrous metal deposits are consistent with those of Mesozoic granites (Figure 10), indicating that gold and nonferrous metal mineralization may be closely related to the Cretaceous magmatic activity. The S isotopic composition in the Liyuan gold deposit obviously shows a larger variation range compared to other deposits in this area. This may be due to some ore-forming fluids from the surrounding rocks.

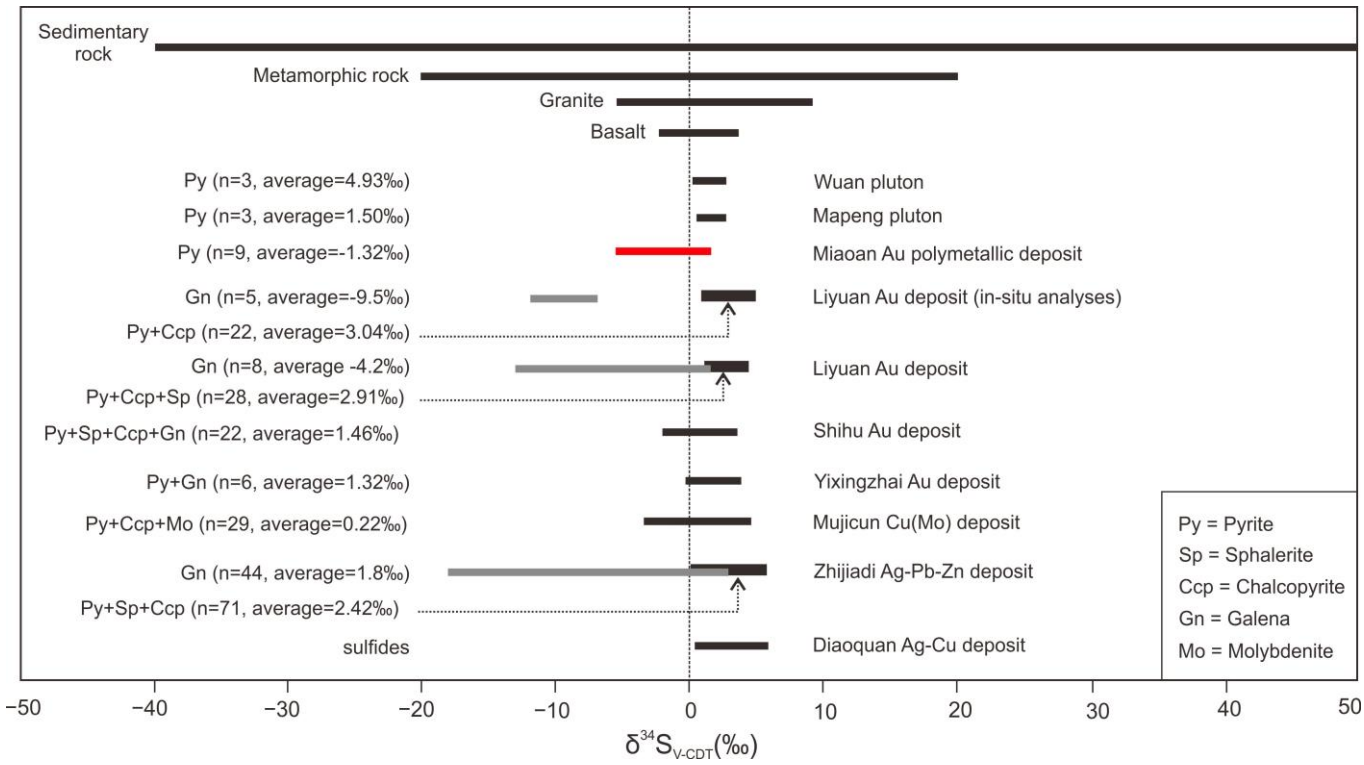

Figure 10. The S isotope compositions of sulfide minerals from the plutons and ore deposits in the central and northern Taihang Mountain regions. Data are sourced from references [13,24,27,63–67,69,94,95].

6.5. Formation Mechanism of the Deposit

The trace element and S–C–O isotope compositions of pyrite grains show that the ore-forming fluid of the Miaoan Au-polymetallic deposit was a Cl-rich reductive fluid. Its ore-forming materials were mainly derived from mantle magma sources and were contaminated by crustal materials. The Mesozoic complex intrusions (e.g., the Laiyuan complex intrusion) in the NTM region show a crust-mantle mixing genesis. The magmatic activity during this period was spatiotemporally related to the mineralization of Au, Cu, and Mo in this region. Importantly, eastern China experienced drastic tectonic transitions and the destruction of the North China Craton in the Mesozoic [96–99]. The destruction of the North China Craton, Mesozoic magmatism, and large-scale gold mineralization in the NTM region, which share the same peak age, suggest a close genetic relationship between them [2,3,100]. Thus, we propose that the Miaoan Au-polymetallic deposit is a decratonic gold deposit. The destruction of the North China Craton induced the upwelling of asthenospheric materials, which resulted in intense crust-mantle interactions, large-scale Mesozoic magmatic activity, and simultaneous Au mineralization around the NCC destruction zone during the Mesozoic (Figure 11).

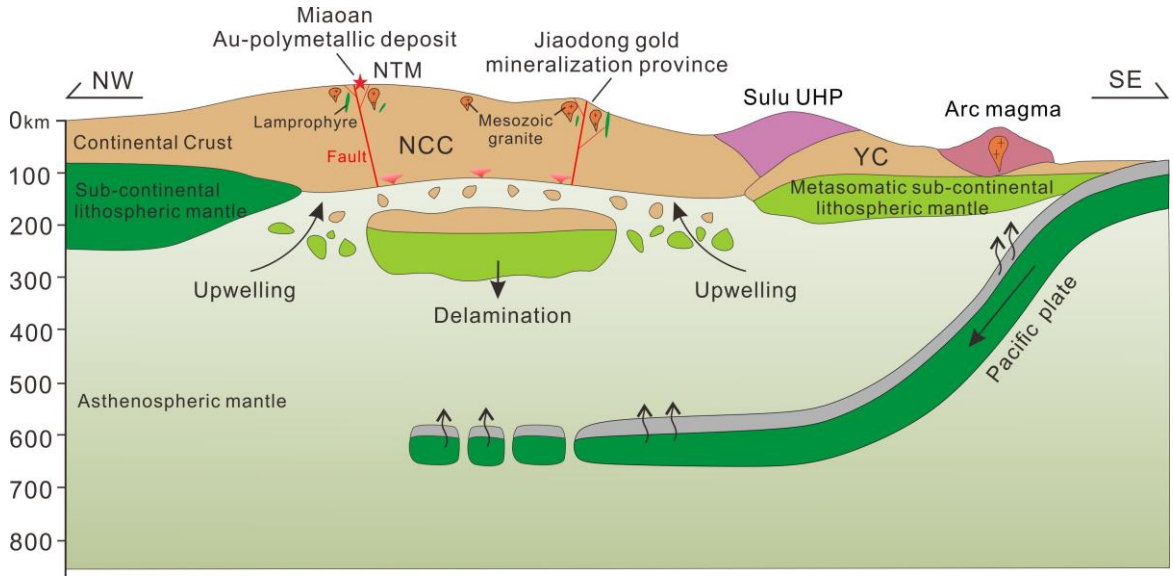

Figure 11. Schematic model of the Cretaceous tectonic evolution, magmatism, and mineralization in the northern Taihang Mountains, North China Craton. NCC: North China Craton; YC: Yangtze Craton; NTM: Northern Taihang Mountain.

7. Conclusions

(1) The Au mineralization shows a close spatial relationship with skarn-type Cu–Fe and Cu–Zn mineralization in the Miaoan Au-polymetallic deposit.
(2) The Miaoan Au-polymetallic deposit was formed at 129.5 ± 2.4 Ma as indicated by the pyrite Rb–Sr isochron age, which is consistent with the age of magmatic rocks exposed in this deposit, suggesting a genetic relationship between them.
(3) Large amounts of mantle-derived materials were involved in ore-forming fluids, as indicated by the S isotopes of pyrites and the C–O isotopes of calcites and ores.
(4) The destruction of the North China Craton induced the upwelling of asthenospheric materials, which resulted in intense crust-mantle interactions, magmatic activity, and Au mineralization.

Author Contributions: Conceptualization, J.L. and L.Z.; validation, N.L. and M.W.; formal analysis, J.L., L.Z., N.L. and Y.S.; investigation, J.L., M.W., Z.T., P.Z. and G.W.; resources, Z.T., P.Z. and G.W.; writing—original draft preparation, J.L. and L.Z.; writing—review and editing, J.L. and L.Z.; funding acquisition, J.L. All authors have read and agreed to the published version of the manuscript.

Funding: This research was funded by Key Projects of Science and Technology Research in Universities of Hebei Province (ZD2021018), Hebei Natural Science Foundation (D2020403061), Opening Fund of Provincial Key Lab of Applied Nuclear Techniques in Geosciences (gnzds202002), and Opening Foundation of Hebei Key Laboratory of Strategic Critical Mineral Resources (HGU-RGM2010).

Data Availability Statement: All data, models, or codes that support the findings of this study are available from the corresponding author upon reasonable request.

Conflicts of Interest: The authors declare no conflict of interest.

References

1. Hou, Z.Q.; Li, Q.Y.; Gao, Y.F.; Lu, Y.J.; Yang, Z.M.; Wang, R.; Shen, Z.C. Lower-crustal magmatic hornblendite in North China Craton: Insight into the genesis of porphyry Cu deposits. *Econ. Geol.* **2015**, *110*, 1879–1904. [CrossRef]
2. Zhu, R.X.; Fan, H.R.; Li, J.W.; Meng, Q.R.; Li, S.R.; Zeng, Q.D. Decratonic gold deposits. *Sci. China-Earth Sci.* **2015**, *58*, 1523–1537. [CrossRef]
3. Zhu, R.X.; Sun, W.D. The big mantle wedge and decratonic gold deposits. *Sci. China-Earth Sci.* **2021**, *64*, 1451–1462. [CrossRef]
4. Liu, Z.; Mao, X.; Jedemann, A.; Bayless, R.C.; Deng, H.; Chen, J.; Xiao, K. Evolution of pyrite compositions at the Sizhuang gold deposit, Jiaodong Peninsula, eastern China: Implications for the genesis of Jiaodong-type orogenic gold mineralization. *Minerals* **2021**, *11*, 344. [CrossRef]

5. Li, S.R.; Santosh, M. Metallogeny and craton destruction: Records from the North China Craton. *Ore Geol. Rev.* **2014**, *56*, 376–414. [CrossRef]
6. Li, J.W.; Bi, S.J.; Selby, D.; Chen, L.; Vasconcelos, P.; Thiede, D.; Zhou, M.F.; Zhao, X.F.; Li, Z.K.; Qiu, H.N. Giant Mesozoic gold provinces related to the destruction of the North China Craton. *Earth Planet. Sci. Lett.* **2012**, *349*, 26–37. [CrossRef]
7. Chen, B.H.; Deng, J.; Ji, X.Z. Time limit of gold mineralization in Muping-Rushan belt, eastern Jiaodong Peninsula, China: Evidence from muscovite Ar-Ar dating. *Minerals* **2022**, *12*, 278. [CrossRef]
8. Li, S.S.; Li, L.; Li, S.R.; Santosh, M.; Alam, M. Age and mineralization processes of decratonic lode gold deposits in the southern North China Craton: Constraints from trace elements, in-situ S-Pb isotopes and Rb-Sr geochronology of pyrite from the Chen'er gold deposit. *Ore Geol. Rev.* **2022**, *145*, 104888. [CrossRef]
9. Cai, Y.C.; Fan, H.R.; Santosh, M.; Hu, F.F.; Yang, K.F.; Li, X.H. Decratonic gold mineralization: Evidence from the Shangzhuang gold deposit, eastern North China Craton. *Gondwana Res.* **2018**, *54*, 1–22. [CrossRef]
10. Song, M.C.; Xue, G.Q.; Liu, H.B.; Li, Y.X.; He, C.Y.; Wang, H.J.; Wang, B.; Song, Y.X.; Li, S.Y. A geological-geophysical prospecting model for deep-seated gold deposits in the Jiaodong Peninsula, China. *Minerals* **2021**, *11*, 1393. [CrossRef]
11. Li, C.P.; Shen, J.F.; Li, S.R.; Liu, Y.; Liu, F.X. In-situ LA-ICP-MS trace elements analysis of pyrite and the physicochemical conditions of telluride formation at the Baiyun gold deposit, North East China: Implications for gold distribution and deposition. *Minerals* **2019**, *9*, 129. [CrossRef]
12. Goldfarb, R.J.; Groves, D.I.; Gardoll, S. Orogenic gold and geologic time: A global synthesis. *Ore Geol. Rev.* **2001**, *18*, 1–75. [CrossRef]
13. Li, S.R.; Santosh, M.; Zhang, H.F.; Shen, J.F.; Dong, G.C.; Wang, J.Z.; Zhang, J.Q. Inhomogeneous lithospheric thinning in the central North China Craton: Zircon U-Pb and S-He-Ar isotopic record from magmatism and metallogeny in the Taihang Mountains. *Gondwana Res.* **2013**, *23*, 141–160. [CrossRef]
14. Deng, J.; Wang, C.M.; Bagas, L.; Santosh, M.; Yao, E.Y. Crustal architecture and metallogenesis in the south-eastern North China Craton. *Earth-Sci. Rev.* **2018**, *182*, 251–272. [CrossRef]
15. Deng, J.; Wang, Q.F.; Santosh, M.; Liu, X.F.; Liang, Y.Y.; Yang, L.Q.; Zhao, R.; Yang, L. Remobilization of metasomatized mantle lithosphere: A new model for the Jiaodong gold province, eastern China. *Miner. Depos.* **2020**, *55*, 257–274. [CrossRef]
16. Song, M.C.; Li, S.Z.; Santosh, M.; Zhao, S.J.; Yu, S.; Yi, P.H.; Cui, S.X.; Lv, G.X.; Xu, J.X.; Song, Y.X.; et al. Types, characteristics and metallogenesis of gold deposits in the Jiaodong Peninsula, eastern North China Craton. *Ore Geol. Rev.* **2015**, *65*, 612–625. [CrossRef]
17. Sun, W.D. Decratonic gold deposits: A new concept and new opportunities. *Natl. Sci. Rev.* **2015**, *2*, 248–249. [CrossRef]
18. Li, L.; Santosh, M.; Li, S.R. The 'Jiaodong type' gold deposits: Characteristics, origin and prospecting. *Ore Geol. Rev.* **2015**, *65*, 589–611. [CrossRef]
19. Song, M.-C.; Li, J.; Yu, X.-F.; Song, Y.-X.; Ding, Z.-J.; Li, S.-Y. Metallogenic characteristics and tectonic setting of the Jiaodong gold deposit, China. *Solid Earth Sci.* **2021**, *6*, 385–405. [CrossRef]
20. Sun, W.D.; Ding, X.; Hu, Y.H.; Li, X.H. The golden transformation of the Cretaceous plate subduction in the west Pacific. *Earth Planet. Sci. Lett.* **2007**, *262*, 533–542. [CrossRef]
21. Sun, W.D.; Li, S.; Yang, X.Y.; Ling, M.X.; Ding, X.; Duan, L.A.; Zhan, M.Z.; Zhang, H.; Fan, W.M. Large-scale gold mineralization in eastern China induced by an early Cretaceous clockwise change in Pacific plate motions. *Int. Geol. Rev.* **2013**, *55*, 311–321. [CrossRef]
22. Deng, J.; Liu, X.F.; Wang, Q.F.; Pan, R.G. Origin of the Jiaodong-type Xinli gold deposit, Jiaodong Peninsula, China: Constraints from fluid inclusion and C-D-O-S-Sr isotope compositions. *Ore Geol. Rev.* **2015**, *65*, 674–686. [CrossRef]
23. Groves, D.I.; Santosh, M. The giant Jiaodong gold province: The key to a unified model for orogenic gold deposits? *Geosci. Front.* **2016**, *7*, 409–417. [CrossRef]
24. Peng, N.; Shao, Y.; Liu, Z.; Wang, C. Metallogenic mechanism of Yixingzhai gold ore field in Fanshi county, Shanxi province: Evidences from isotopes and fluid inclusion. *Chin. J. Nonferrous Met.* **2017**, *27*, 305–317.
25. Zhang, J.Q.; Li, S.R.; Santosh, M.; Lu, J.; Wang, C.L. Metallogenesis of precambrian gold deposits in the Wutai greenstone belt: Constrains on the tectonic evolution of the North China Craton. *Geosci. Front.* **2018**, *9*, 317–333. [CrossRef]
26. Zhang, J.Q.; Li, S.R.; Santosh, M.; Niu, S.D.; Li, Q.; Lu, J. The magmatic-hydrothermal mineralization systems of the Yixingzhai and Xinzhuang gold deposits in the central North China Craton. *Ore Geol. Rev.* **2017**, *88*, 416–435. [CrossRef]
27. Zhu, X.Q.; Wang, J.B.; Pang, Z.S.; Zhen, S.M.; Yang, F.; Xue, J.L.; Jia, H.X.; Shi, G.Y. Ore geology, fluid inclusion microthermometry and H-O-S isotopes of the Liyuan gold deposit, central Taihang mountains, North China Craton. *Minerals* **2019**, *9*, 606. [CrossRef]
28. Kusky, T.M.; Windley, B.F.; Zhai, M.G. Tectonic evolution of the North China block: From orogen to craton to orogen. *Mesoz. Sub-Cont. Lithospheric Thinning Under East. Asia* **2007**, *280*, 1–34. [CrossRef]
29. Zhai, M.G. Lower crust and lithospheric mantle beneath the North China Craton before the Mesozoic lithospheric disruption. *Acta Petrol. Sin.* **2008**, *24*, 2185–2204.
30. Zhai, M.-G.; Santosh, M. The early Precambrian odyssey of the North China Craton: A synoptic overview. *Gondwana Res.* **2011**, *20*, 6–25. [CrossRef]
31. Tang, L.; Santosh, M. Neoarchean-Paleoproterozoic terrane assembly and Wilson cycle in the North China Craton: An overview from the central segment of the Trans-North China Orogen. *Earth-Sci. Rev.* **2018**, *182*, 1–27. [CrossRef]
32. Zhu, R.X.; Yang, J.H.; Wu, F.Y. Timing of destruction of the North China Craton. *Lithos* **2012**, *149*, 51–60. [CrossRef]

33. Wu, F.-Y.; Yang, J.-H.; Xu, Y.-G.; Wilde, S.A.; Walker, R.J. Destruction of the North China Craton in the Mesozoic. *Annu. Rev. Earth Planet. Sci.* **2019**, *47*, 173–195. [CrossRef]
34. Chu, X.L.; Sun, J.G.; Sun, F.T.; Mei, Y.X.; Liu, Y.; Men, L.; Zhao, K.Q.; Zhang, X.T. Petrogenesis of the early Cretaceous Hongshan complex in the southern Taihang Mountains: Constraints from element geochemistry, zircon U-Pb geochronology and Hf isotopes. *Minerals* **2021**, *11*, 1111. [CrossRef]
35. Gao, Y.F.; Santosh, M.; Wei, R.H.; Ma, G.X.; Chen, Z.K.; Wu, J.L. Origin of high Sr/Y magmas from the northern Taihang Mountains: Implications for Mesozoic porphyry copper mineralization in the North China Craton. *J. Asian Earth Sci.* **2013**, *78*, 143–159. [CrossRef]
36. Wu, F.Y.; Lin, J.Q.; Wilde, S.A.; Zhang, X.O.; Yang, J.H. Nature and significance of the early Cretaceous giant igneous event in eastern China. *Earth Planet. Sci. Lett.* **2005**, *233*, 103–119. [CrossRef]
37. Wu, F.Y.; Xu, Y.G.; Gao, S.; Zheng, J.P. Lithospheric thinning and destruction of the North China Craton. *Acta Petrol. Sin.* **2008**, *24*, 1145–1174.
38. Yang, J.H.; Wu, F.Y.; Wilde, S.A. A review of the geodynamic setting of large-scale late Mesozoic gold mineralization in the North China Craton: An association with lithospheric thinning. *Ore Geol. Rev.* **2003**, *23*, 125–152. [CrossRef]
39. Zhu, R.X.; Chen, L.; Wu, F.Y.; Liu, J.L. Timing, scale and mechanism of the destruction of the North China Craton. *Sci. China-Earth Sci.* **2011**, *54*, 789–797. [CrossRef]
40. Cai, J.; Yan, G.; Chang, Z.; Wang, X.; Shao, H.; Chu, Z. Petrological and geochemical characteristics of the Wanganzhen complex and discussion on its genesis. *Acta Petrol. Sin.* **2003**, *19*, 81–92.
41. Shen, Z.C.; Hou, Z.Q.; Yu, F.; Chen, Z.K.; Li, Q.Y.; Ma, G.X.; Ge, F.; Wang, Z.M. Shrimp zircon U-Pb ages and Hf isotopes of the intermediate-acidic rocks of Wanganzhen complex in northern part of Taihang Mountains and their geological implications. *Acta Petrol. Sin.* **2015**, *31*, 1409–1420.
42. Xue, F.; Santosh, M.; Kim, S.W.; Tsunogae, T.; Yang, F. Thermo-mechanical destruction of Archean cratonic roots: Insights from the Mesozoic Laiyuan granitoid complex, North China Craton. *Lithos* **2021**, *400–401*, 106394. [CrossRef]
43. Zhang, J.Q.; Li, S.R.; Santosh, M.; Li, Q.; Niu, S.D.; Li, Z.D.; Zhang, X.G.; Jia, L.B. Timing and origin of Mesozoic magmatism and metallogeny in the Wutai-Hengshan region: Implications for destruction of the North China Craton. *J. Asian Earth Sci.* **2015**, *113*, 677–694. [CrossRef]
44. Qu, K.; Dong, G.; Li, S.; Shen, J.; Wang, Y.; Wang, X.; Luo, W. Lithogeochemistry and Sr-Nd-Pb isotopic characteristics of Mujicun porphyry Cu-Mo deposit in Taihang Mountains and their significances. *Geoscience* **2014**, *28*, 449–460.
45. Lüders, V.; Ziemann, M. Possibilities and limits of infrared light microthermometry applied to studies of pyrite-hosted fluid inclusions. *Chem. Geol.* **1999**, *154*, 169–178. [CrossRef]
46. Yang, J.-H.; Zhou, X.-H. Rb-Sr, Sm-Nd, and Pb isotope systematics of pyrite: Implications for the age and genesis of lode gold deposits. *Geology* **2001**, *29*, 711–714. [CrossRef]
47. Li, Q.-L.; Chen, F.; Yang, J.-H.; Fan, H.-R. Single grain pyrite Rb–Sr dating of the linglong gold deposit, eastern China. *Ore Geol. Rev.* **2008**, *34*, 263–270. [CrossRef]
48. Dong, L.; Wan, B.; Yang, W.; Deng, C.; Chen, Z.; Yang, L.; Cai, K.; Xiao, W. Rb-Sr geochronology of single gold-bearing pyrite grains from the Katbasu gold deposit in the south Tianshan, China and its geological significance. *Ore Geol. Rev.* **2018**, *100*, 99–110. [CrossRef]
49. Zhang, P.; Kou, L.; Bi, Z.; Han, R.; Zhao, Y.; Sha, D. Rb–Sr dating of gold-bearing pyrite in the Jinchang porphyry Cu–Au deposit, Heilongjiang province, NE China. *Resour. Geol.* **2018**, *68*, 446–454. [CrossRef]
50. Wang, Y.; Zeng, Q.; Liu, J.; Wu, L.; Qin, K. Porphyry Mo and epithermal Au–Ag–Pb–Zn mineralization in the Zhilingtou polymetallic deposit, South China. *Miner. Depos.* **2020**, *55*, 1385–1406. [CrossRef]
51. Wang, C.; Deng, J.; Santosh, M.; Carranza, E.J.M.; Gong, Q.; Guo, C.; Xia, R.; Lai, X. Timing, tectonic implications and genesis of gold mineralization in the Xincheng gold deposit, china: C–H–O isotopes, pyrite Rb–Sr and zircon fission track thermochronometry. *Ore Geol. Rev.* **2015**, *65*, 659–673. [CrossRef]
52. Ludwig, K.R. Isoplot 3.0: A geochronological toolkit for microsoft excel. Berkeley geochronology center special publication. *US Geol. Sur. Open File Rep.* **2003**, *39*, 91–445.
53. Wang, Y.X.; Yang, J.D.; Chen, J.; Zhang, K.J.; Rao, W.B. The Sr and Nd isotopic variations of the Chinese Loess Plateau during the past 7 Ma: Implications for the East Asian winter monsoon and source areas of loess. *Palaeogeogr. Palaeoclimatol. Palaeoecol.* **2007**, *249*, 351–361. [CrossRef]
54. Chen, B.H.; Wang, Z.L.; Li, H.L.; Li, J.K.; Li, J.L.; Wang, G.Q. Evolution of ore fluid of the Taishang gold deposit, Jiaodong: Constraints on REE and trace element component of auriferous pyrite. *Acta Petrol. Sin.* **2014**, *30*, 2518–2532.
55. Guo, L.; Huang, C.; Zhang, L.; Chen, B.; Li, R.; Liu, Y. Source of ore-forming fluids in the Luoshan gold deposit, Jiaodong:Constrains from REE and trace element features of auriferous pyrite in the altered-rock type and auriferous quartz vein type ores. *Geoscience* **2019**, *33*, 121–136.
56. Li, J.; Song, M.C.; Liang, J.L.; Jiang, M.Y.; Li, S.Y.; Ding, Z.J.; Su, F. Source of ore-forming fluids of the Jiaojia deeply seated gold deposit: Evidences from trace elements and Sulfur-Helium-Argon isotopes of pyrite. *Acta Petrol. Sin.* **2020**, *36*, 297–313.
57. Xue, J.L.; Li, S.R.; Pang, Z.S.; Tao, W.; Sun, W.Y.; Chen, H.; Zhang, Y.Q. Ore-forming fluids, sources of materials in the Denggezhuang gold deposit, Jiaodong Penisula and implications for ore genesis. *Acta Petrol. Sin.* **2018**, *34*, 1453–1468.

58. Sun, S.S.; McDonough, W.S. *Chemical and Isotopic Systematics of Oceanic Basalts: Implications for Mantle Composition and Processes*; Geological Society Special Publication: London, UK, 1989; Volume 42, pp. 313–345.
59. Rudnick, R.L.; Gao, S. Composition of the continental crust. *Treatise Geochem.* **2003**, *3*, 1–64.
60. Bajwah, Z.U.; Seccombe, P.K.; Offler, R. Trace element distribution, Co:Ni ratios and genesis of the big cadia iron-copper deposit, new south wales, australia. *Miner. Depos.* **1987**, *22*, 292–300. [CrossRef]
61. Brill, B.A. Trace-element contents and partitioning of elements in ore minerals from the CSA Cu-Pb-Zn deposit, Australia, and implications for ore genesis. *Can. Mineral.* **1989**, *27*, 263–274.
62. Chao, C.; Shu-yin, N.I.U.; Bao-de, W.; Ai-qun, S.U.N.; Bao-jun, M.A.; Wen-xue, W.; Yin-cang, G.A.O. A tentative discussion on ore-forming material sources and mineralization of the Shihu gold deposit in western Hebei province. *Geol. China* **2009**, *36*, 1340–1349.
63. Cui, Y. The chemical composition and its genetic significance of the pyrite in Tuling–Shihu gold deposits. *Acta Petrol. Mineral.* **1993**, *12*, 371–381.
64. Chen, C.; Wang, B.; Niu, S.; Zhang, F.; Ma, B.; Zhang, J.; Sun, A.; Wang, H.; Ma, G.; Chen, Z.; et al. Discussion on the ore-forming material sources of Mujicun copper (molybdenum)polymetallic orefield in Laiyuan county, Hebei province, China. *J. Jilin Univ. Earth Sci. Ed.* **2015**, *45*, 106–118.
65. Dong, G.C.; Santosh, M.; Li, S.R.; Shen, J.F.; Mo, X.X.; Scott, S.; Qu, K.; Wang, X. Mesozoic magmatism and metallogenesis associated with the destruction of the North China Craton: Evidence from U-Pb geochronology and stable isotope geochemistry of the Mujicun porphyry Cu-Mo deposit. *Ore Geol. Rev.* **2013**, *53*, 434–445. [CrossRef]
66. Ma, G.X. Geological characteristics and metallogenic model of copper deposit at Muji village of Laiyuan county, Hebei province. *J. Geol. Miner. Resour. North China* **1997**, *12*, 52–66.
67. Zhen, S.; Pang, Z.; Zhu, X.; Xue, J.; Fang, Y.; Jia, H.; Shi, G.; Wang, D.; Zha, Z.; Song, X. The characteristics of trace elements and S, Pb, He and Ar isotopes in the Liyuan gold deposit in Shanxi province, and their significance. *Earth Sci. Front.* **2020**, *27*, 373–390.
68. Chen, C.; Niu, S.; Wang, F.; Zhang, F.; Zhang, Q.; Ma, B.; Sun, A.; Zhang, J.; Cao, Y.; Zhang, X. Timing of mineralization at the Shihu gold deposit in the middle segment of the Taihang Mountain, China. *Acta Geochim.* **2018**, *37*, 80–89. [CrossRef]
69. Chen, B.; Chen, Z.C.; Jahn, B.M. Origin of mafic enclaves from the Taihang Mesozoic Orogen, North China Craton. *Lithos* **2009**, *110*, 343–358. [CrossRef]
70. Gao, Y.F.; Santosh, M.; Hou, Z.Q.; Wei, R.H.; Ma, G.X.; Chen, Z.K.; Wu, J.L. High Sr/Y magmas generated through crystal fractionation: Evidence from Mesozoic volcanic rocks in the northern Taihang Orogen, North China Craton. *Gondwana Res.* **2012**, *22*, 152–168. [CrossRef]
71. Song, Y.; Ding, H.Y.; Qu, X.M.; Wang, R.J.; Zhou, W.; Wang, S.Z. Re-Os and U-Pb geochronology of the Dawan Mo-Zn-Fe deposit in northern Taihang Mountains, China. *Resour. Geol.* **2014**, *64*, 117–135. [CrossRef]
72. Xue, F.; Santosh, M.; Tsunogae, T.; Yang, F. Geochemical and isotopic imprints of early Cretaceous mafic and felsic dyke suites track lithosphere-asthenosphere interaction and craton destruction in the North China Craton. *Lithos* **2019**, *326*, 174–199. [CrossRef]
73. Bi, X.W.; Hu, R.Z.; Peng, J.T.; Li, H.L.; Hu, X.Y. REE and HFSE geochemical characteristics of pyrites in Yao'an gold deposit in western Yunnan, China: Tracing ore forming fluid signatures. *Geochim. Cosmochim. Acta* **2008**, *72*, A81.
74. Liang, J.L.; Li, J.; Liu, X.M.; Zhai, W.; Huang, Y.; Zhao, J.; Sun, W.D.; Song, M.C.; Li, J.Z. Multiple element mapping and in-situ S isotopes of Au-carrying pyrite of Shuiyindong gold deposit, southwestern China using NanoSIMS: Constraints on Au sources, ore fluids, and mineralization processes. *Ore Geol. Rev.* **2020**, *123*, 103576. [CrossRef]
75. Zhang, W.-D.; Li, B.; Lu, A.-H.; Zhao, K.-D.; Elatikpo, S.M.; Chen, X.-D.; Zhu, L.; Yu, M. In-situ pyrite trace element and sulfur isotope characteristics and metallogenic implications of the Qixiashan Pb-Zn-Ag polymetallic deposit, eastern China. *Ore Geol. Rev.* **2022**, *144*, 104849. [CrossRef]
76. Zhang, Y.; Zhen, S.; Wang, D.; Liu, J.; Wang, J.; Zha, Z.; Bai, H. In situ trace elements and sulfur isotopes of sulfides in the Dabaiyang Te-Au deposit, Hebei province, China: Implications for Au remobilization from pyrite. *Ore Geol. Rev.* **2022**, *140*, 104626. [CrossRef]
77. Sun, G.; Zeng, Q.; Zhou, L.; Wang, Y.; Chen, P. Trace element contents and in situ sulfur isotope analyses of pyrite in the Baiyun gold deposit, NE China: Implication for the genesis of intrusion-related gold deposits. *Ore Geol. Rev.* **2020**, *118*, 103330. [CrossRef]
78. Haas, J.R.; Shock, E.L.; Sassani, D.C. Rare-earth elements in hydrothermal systems—Estimates of standard partial molal thermodynamic properties of aqueous complexes of the rare-earth elements at high-pressures and temperatures. *Geochim. Cosmochim. Acta* **1995**, *59*, 4329–4350. [CrossRef]
79. Keppler, H. Constraints from partitioning experiments on the composition of subduction-zone fluids. *Nature* **1996**, *380*, 237–240. [CrossRef]
80. Oreskes, N.; Einaudi, M.T. Origin of rare-earth element-enriched hematite breccias at the Olympic-Dam Cu-U-Au-Ag deposit, Roxby Downs, South Australia. *Econ. Geol. Bull. Soc. Econ. Geol.* **1990**, *85*, 1–28. [CrossRef]
81. Bralia, A.; Sabatini, G.; Troja, F. A revaluation of the Co/Ni ratio in pyrite as geochemical tool in ore genesis problems. *Miner. Depos.* **1979**, *14*, 353–374. [CrossRef]
82. Bau, M.; Dulski, P. Comparative-study of yttrium and rare-earth element behaviors in fluorine-rich hydrothermal fluids. *Contrib. Mineral. Petrol.* **1995**, *119*, 213–223. [CrossRef]
83. Yaxley, G.M.; Green, D.H.; Kamenetsky, V. Carbonatite metasomatism in the southeastern Australian lithosphere. *J. Petrol.* **1998**, *39*, 1917–1930. [CrossRef]

84. Zheng, Y.F. Carbon and oxygen isotopic convariations in hydrothermal calcite during of CO_2: A quantitative evaluation and application to Kushikino gold mining area in Japan. *Miner. Depos.* **1990**, *25*, 246–250. [CrossRef]
85. Zheng, Y.F.; Hoefs, J. Carbon and oxygen isotopic covariations in hydrothermal calcites—Theoretical modeling on mixing processes and application to Pb-Zn deposits in the Harz mountains, Germany. *Miner. Depos.* **1993**, *28*, 79–89.
86. Taylor, B.E. Magmatic volatiles; isotopic variation of C, H, and S. *Rev. Mineral. Geochem.* **1986**, *16*, 185–225.
87. Veizer, J.; Holser, W.; Wilgus, C. Correlation of $^{13}C/^{12}C$ and $^{34}S/^{32}S$ secular variations. *Geochim. Cosmochim. Acta* **1980**, *44*, 579–587. [CrossRef]
88. Ohmoto, H. Systematics of sulfur and carbon isotopes in hydrothermal ore-deposits. *Econ. Geol.* **1972**, *67*, 551–578. [CrossRef]
89. Hoefs, J. *Stable Isotope Geochemistry*; Springer: Berlin/Heidelberg, Germany, 1997; Volume 201.
90. Wu, K.; Hu, R.; Bi, X.; Peng, J. An oxygen and carbon isotope study on the formation mode of calcite in Beiya gold deposit, west Yunnan province, China. *Acta Mineral. Sin.* **2010**, *30*, 463–469.
91. Li, J.; Li, C.-Y.; Liang, J.-L.; Song, M.-C.; Zhang, L.-P.; Song, Y.-X. Mineralization of the Shangjiazhuang Mo deposit in the Jiaodong Peninsula, China: Constraints from S–H–O isotopes and fluid inclusions. *Solid Earth Sci.* **2021**, *6*, 370–384. [CrossRef]
92. Liang, J.L.; Li, J.; Sun, W.D.; Zhao, J.; Zhai, W.; Huang, Y.; Song, M.C.; Ni, S.J.; Xiang, Q.R.; Zhang, J.C.; et al. Source of ore-forming fluids of the Yangshan gold field, western Qinling orogen, China: Evidence from microthermometry, noble gas isotopes and in situ sulfur isotopes of Au-carrying pyrite. *Ore Geol. Rev.* **2019**, *105*, 404–422. [CrossRef]
93. Ohmoto, H.; Goldhaber, M. Sulfur and carbon isotopes. In *Geochemistry of Hydrothermal Ore Deposits*; John Wiley & Sons: Hoboken, NJ, USA, 1997; pp. 517–612.
94. Wang, Q.C.; Ma, J.L.; Zhang, J.Z. The geochemical characteristics of the Mapeng gold mine at the boundary between Lingshou and Fuping in Hebei province and the origin of the deposits. *Geochimica* **1995**, *24*, 57–68.
95. Zhang, B.; Zhao, G.; Ma, G. *The Metallogenetic System and Ore-Forming Models of the Main Metallogeneic Belts in Hebei Province*; Petroleum Industrial Publishing, House: Beijing, China, 1996.
96. Mao, J.W.; Wang, Y.T.; Zhang, Z.H.; Yu, J.J.; Niu, B.G. Geodynamic settings of Mesozoic large-scale mineralization in North China and adjacent areas—Implication from the highly precise and accurate ages of metal deposits. *Sci. China Ser. D-Earth Sci.* **2003**, *46*, 838–851. [CrossRef]
97. Zhang, Z.-K.; Ling, M.-X.; Lin, W.; Sun, M.; Sun, W. "Yanshanian movement" induced by the westward subduction of the paleo–Pacific plate. *Solid Earth Sci.* **2020**, *5*, 103–114. [CrossRef]
98. Hou, Q.-L.; Liu, Q.; Lin, W.; Xu, D.-R.; He, M.; Wang, Z.-L.; Wei, W.; Guo, Q.-Q. Mesozoic tectonic regime and evolution of eastern China: A mini-review based on the recent development. *Solid Earth Sci.* **2019**, *4*, 159–165. [CrossRef]
99. Chang, J.; Audetat, A.; Li, J.W. Tectono-magmatic controls on decratonic gold deposits. *Contrib. Mineral. Petrol.* **2021**, *176*, 69. [CrossRef]
100. Li, L.; Li, C.; Li, Q.; Yuan, M.W.; Zhang, J.Q.; Li, S.R.; Santosh, M.; Shen, J.F.; Zhang, H.F. Indicators of decratonic gold mineralization in the North China Craton. *Earth-Sci. Rev.* **2022**, *228*, 103995. [CrossRef]